Journal Pre-proofs

Synergistic surface restructuring and cation mixing via ultrafast Joule heating enhancing ultrahigh-nickel cathodes for advanced lithium-ion batteries

Haoyu Wang, Jinyang Dong, Meng Wang, Yun Lu, Hongyun Zhang, Jinzhong Liu, Yun Liu, Na Liu, Ning Li, Qing Huang, Feng Wu, Yuefeng Su, Lai Chen

PII: S2095-4956(24)00821-0
DOI: https://doi.org/10.1016/j.jechem.2024.11.047
Reference: JECHEM 4290

To appear in: *Journal of Energy Chemistry*

Received Date: 15 October 2024
Revised Date: 16 November 2024
Accepted Date: 17 November 2024

Please cite this article as: H. Wang, J. Dong, M. Wang, Y. Lu, H. Zhang, J. Liu, Y. Liu, N. Liu, N. Li, Q. Huang, F. Wu, Y. Su, L. Chen, Synergistic surface restructuring and cation mixing via ultrafast Joule heating enhancing ultrahigh-nickel cathodes for advanced lithium-ion batteries, *Journal of Energy Chemistry* (2024), doi: https://doi.org/10.1016/j.jechem.2024.11.047

Synergistic surface restructuring and cation mixing via ultrafast Joule heating enhancing ultrahigh-nickel cathodes for advanced lithium-ion batteries

Haoyu Wang [a], Jinyang Dong [a,b,*], Meng Wang [b], Yun Lu [a,b], Hongyun Zhang [a,b], Jinzhong Liu [a,b], Yun Liu [a,b], Na Liu [c], Ning Li [a,b], Qing Huang [a,b], Feng Wu [a,b], Yuefeng Su [a,b,*], Lai Chen [a,b,*]

[a] School of Materials Science and Engineering, Beijing Key Laboratory of Environmental Science and Engineering, Beijing Institute of Technology, Beijing 100081, China

[b] Chongqing Innovation Center, Beijing Institute of Technology, Chongqing 401120, China

[c] Testing Centre of Power Batteries, China North Vehicle Research Institute, Beijing 100072, China

* Corresponding authors.

E-mail addresses: jydong@bit.edu.cn (J. Dong), suyuefeng@bit.edu.cn (Y. Su), chenlai144@sina.com (L. Chen).

Abstract

The implementation of ultrahigh-Ni cathodes in high-energy lithium-ion batteries (LIBs) is constrained by significant structural and interfacial degradation during cycling. In this study, doping-induced surface restructuring in ultrahigh-nickel cathode materials is rapidly facilitated through an ultrafast Joule heating method. Density functional theory (DFT) calculations, synchrotron X-ray absorption spectroscopy (XAS), and single-particle force test confirmed the establishment of a stable crystal framework and lattice oxygen, which mitigated H2-H3 phase transitions and improved structural reversibility. Additionally, the Sc doping process exhibits a pinning effect on the grain boundaries, as shown by scanning transmission electron microscopy (STEM), enhancing Li^+ diffusion kinetics and decreasing mechanical strain during cycling. The in situ development of a cation-mixing layer at grain boundaries also creates a robust cathode/electrolyte interphase, effectively reducing interfacial parasitic reactions and transition metal dissolution, as validated by STEM

and time-of-flight secondary ion mass spectrometry (TOF-SIMS). These synergistic modifications reduce particle cracking and surface/interface degradation, leading to enhanced rate capability, structural integrity, and thermal stability. Consequently, the optimized Sc-modified ultrahigh-Ni cathode (Sc-1) exhibits 93.99% capacity retention after 100 cycles at 1 C (25 °C) and 87.06% capacity retention after 100 cycles at 1 C (50 °C), indicating excellent cycling and thermal stability. By presenting a one-step multifunctional modification approach, this research delivers an extensive analysis of the mechanisms governing the structure, microstructure, and interface properties of nickel-rich layered cathode materials (NCMs). These results underscore the potential of ultrahigh-Ni cathodes as viable candidates for advanced lithium-ion batteries (LIBs) in next-generation electric vehicles (EVs).

Keywords:

Lithium-ion batteries; Ultrahigh-nickel layered cathodes; In situ surface doping; Cation mixing layer; Structure and thermal stability

1. Introduction

Lithium-ion batteries (LIBs) play a crucial role in advancing modern energy storage, impacting the development of portable electronics, electric vehicles, and renewable energy technologies [1-3]. These batteries are recognized for their efficiency, high energy density, and rechargeability. The cathode is essential in determining both the energy density and cost-effectiveness of LIBs, with various materials, including layered, spinel, and olivine structures, under investigation [4-6]. Ternary cathode materials within the layered category have notably enhanced next-generation batteries due to their low cost, high energy density, and rapid charge capabilities. Nevertheless, despite advancements, Ni-rich cathodes, with capacities nearing about 200 mAh g^{-1}, remain insufficient to meet industry demands, highlighting the need for further innovation in cathode material development [7-9]. Elevated nickel concentrations in cathode materials significantly aggravate volumetric and surface degradation. Considerable lattice expansion and contraction in nickel-rich cathodes during cycling induce mechanical stresses and strains, resulting in lattice distortions and microstructural changes that lead to microcracks, thereby compromising cathode integrity. Furthermore, the reactivity of charged Ni^{4+} ions leads to adverse electrolyte interactions, forming a cathode-electrolyte interface (CEI) layer that consumes Li^{+} ions and increases interfacial impedance, ultimately causing irreversible capacity loss [10-12]. These performance limitations associated with ultrahigh-nickel lithium-ion batteries result in significantly reduced cycle life and safety, particularly at elevated temperatures and high charge cutoff voltages.

The performance decline of ultrahigh nickel cathodes is closely associated with intergranular cracking, which facilitates increased electrolyte infiltration into particle interiors, thereby exacerbating interfacial side reactions. This interaction leads to surface degradation and impedance growth over extended cycling [13-15]. To mitigate these challenges, various strategies, including elemental doping, surface coating, and morphological engineering, have been investigated. Surface treatments employing materials such as oxides, fluorides, and phosphates have demonstrated effectiveness in reducing electrolyte erosion, thereby extending battery lifespan [16-18]. However, discrepancies in structure between coatings and substrates may result in interfacial gaps and potential detachment of coatings during prolonged cycling, consequently diminishing their protective effects. Additionally, doping modifications have gained popularity due to their simplicity and effectiveness. The incorporation of ions such as Mg^{2+}, Al^{3+}, Zr^{4+}, and Ti^{4+} raises the thermodynamic barrier against Ni^{2+} ion migration from transition metal sites to lithium-ion sites, thereby enhancing oxygen bonding and improving structural stability while minimizing oxygen loss [19-21]. Previous studies confirmed that niobium-doped high-nickel layered cathode materials can function effectively as highly safe, crack-free cathode materials. However, conventional coating techniques often involve lengthy processes requiring extensive thermal treatments to achieve fine crystalline structures, leading to significant energy consumption and decreased manufacturing efficiency. Therefore, the development of innovative synthesis methods for doping-induced surface

restructuring of ultrahigh-nickel cathode materials is essential.

In traditional doping and coating approaches, the addition of secondary solvent treatment steps often results in the formation of rock salt phases in high-nickel cathode materials. These phases are characterized by lower electronic and ionic conductivities, which significantly impair the capacity and rate capabilities of the material. Moreover, the generation of surface-mixed cationic layers due to solvent treatments in secondary modifications has often been overlooked in prior studies [7,22-24]. Recent research has mainly focused on the advantageous effects of high-valence cation doping, which typically leads to surface mixed-layer restructuring (generally improving performance) while also causing harmful rock salt phase transformations during cycling (which tend to accelerate performance decline). Notably, our previous work has validated the nature of irreversible phase transformation propagation in Ni rich cathode [25]. Recognizing that secondary solvent treatment consistently produces surface mixed phases has led to an exploration of whether the calcination process following this treatment can be effectively managed. Specifically, the goal is to modify the physicochemical properties of the intermediate rock salt layer while incorporating heteroelement doping to tackle the fundamental causes of 'mechano-chemical' failure and address the identified issues. Joule heating has emerged as a rapid and energy-efficient synthesis technique, allowing for the control of material structure and properties through fast reaction kinetics and brief reaction durations [26-28]. Its nonequilibrium characteristics offer promising opportunities for the rapid fabrication of doped, surface-restructured ultrahigh nickel cathode materials.

In this study, the ultrafast sintering capabilities of the "joule heating" system were utilized to develop a pulsed high-temperature sintering approach for fabricating ultrahigh-nickel cathode materials with doping-induced surface restructuring. Initially, scandium (Sc) was gradient-doped onto the surface of the cathode materials, selectively targeting Ni sites within the transition metal layers, effectively mitigating significant lattice alterations and loss of lattice oxygen. Furthermore, the rapid Joule heating rate enabled a nonequilibrium process that resulted in the formation of an artificial Li/Ni cation mixed layer on the particle surfaces. This layer not only preserves the structural support advantages of traditional cation mixing but also addresses the low energy barriers associated with Ni migration. These synergistic improvements greatly enhance the cycle stability, rate capability, and thermal stability of the novel high-nickel cathode material. Additionally, density functional theory (DFT) calculations were employed to analyze and clarify the doping mechanism and the critical role of Sc within the structure, while in situ X-ray diffraction (XRD) characterization and X-ray absorption spectroscopy (XAS) techniques provided insights into the crystal structural changes during operation, establishing a foundation for understanding the structural stability of high-nickel cathode materials. This research emphasizes the importance of surface doping and mixed phase control in high-nickel cathode materials, offering a universal and practical strategy to combat rapid mechanochemical degradation and providing strong technological support for

their potential industrial application.

2. Results and discussion

$Sc(NO_3)_3$ exhibits significant advantages in terms of solubility and melting point. Its low melting point facilitates easier reaction with Ni rich materials during the Joule heating process, while its high solubility ensures effective dispersion of scandium ions, promoting enhancements in material properties. Additionally, its moderate cost contributes to its practicality in real-world applications. Fig. 1(a) presents a schematic illustration of the Joule-heating synthesis method employed for the production of the heterostructured cathode material. The precursor for this material was initially synthesized using a conventional combustion technique (refer to the Experimental Section for additional details in Supporting Information). The creation of ultrahigh nickel cathode materials involves the treatment with $Sc(NO_3)_3$, followed by a Joule-heating process that promotes doping-induced surface restructuring. The Joule-heating method is defined by rapid ramping and quenching rates of around 300 °C s^{-1} (Fig. S1), allowing for a notably short synthesis duration. The nonequilibrium phenomena caused by the swift Joule heating rate facilitate the targeted integration of heteroelements and the simultaneous stabilization of surface mixed phases [29]. This methodology provides an effective design and synthesis approach for the development of high-performance, cost-efficient cathode materials. XRD analyses were conducted to evaluate the influence of Sc doping on the crystal structures of all samples. The XRD findings reveal that the synthesized materials exhibit the hexagonal α-$NaFeO_2$ structure with the *R*-3*m* space group, and no impurity phases are identified. The intensity ratios of $I_{(003)}/I_{(104)}$ for the undoped sample Sc-0 (Fig. 1b) and the Sc-doped sample Sc-1 (Fig. 1c) are 2.12 and 1.87, respectively, indicating enhanced Li^+/Ni^{2+} cation mixing in the Sc-doped samples. This enhancement can be attributed to structural modifications induced by Sc within the lattice of the high-nickel cathode material, particularly in surface and near-surface regions. This substitution lowers the energy barrier for Li^+/Ni^{2+} cation exchange, thus promoting a higher degree of mixing. Additionally, the ultrafast Joule heating process enhances atomic mobility, resulting in a cation-mixing layer on the surface that further stabilizes the structure. Moreover, the distinct splitting of peaks $I_{(006)}/I_{(012)}$ and $I_{(108)}/I_{(110)}$ in the XRD pattern of Sc-0 signifies a well-ordered layered structure in the pristine material [30]. This pattern implies that Li^+/Ni^{2+} disorder increases with higher levels of Sc doping. The detailed crystal structures and lattice parameters were further analyzed using the Rietveld refinement method; the refined patterns are displayed in Table S1. A slight rise in the lattice parameters *a* and *c* following Sc doping indicates the successful incorporation of Sc into the crystal lattice. Additionally, the transition metal contents in the Li layer (Ni/Li) for Sc-0 and Sc-1 are 1.09% and 5.38%, respectively. These values correspond with the observations from the $I_{(003)}/I_{(104)}$ intensity ratios, suggesting that the substitution of Sc on the surface and the Joule-heating process facilitate the increased formation of Ni^{2+}. Notably, the ultrafast Joule-heating process,

characterized by extremely rapid heating and cooling rates, creates non-equilibrium conditions that significantly influence the oxidation state of nickel and the structural integrity of the cathode material. The enhanced formation of Ni^{2+} during the Joule-heating process is driven by the creation of oxygen vacancies, Sc-induced modification of the local electronic structure, and the non-equilibrium kinetics of rapid thermal cycling.

Electrical conductivity is critical for assessing cathode performance, and powder resistivity measurements offer key electrochemical insights. Using the PRCD3100 system (IEST, Fig. 1d), the powder resistivity decreased with increasing testing pressure. The modified electrical resistivity of Sc-1 demonstrates the potential of Sc surface doping to improve the electrochemical performance. The morphology of the synthesized materials was investigated using scanning electron microscopy (SEM). Fig. 1(e–h) illustrates that all samples are composed of about 10 μm spherical secondary particles formed from closely packed primary particles, indicating that surface Sc doping has a negligible effect on their overall morphology. Fig. S2 displays energy dispersive spectroscopy (EDS) mapping for Sc-1, revealing a uniform distribution of Ni, Co, Mn, Sc, and O across the surface, with no significant variations. Although the Sc content is lower, its distribution is consistent with that of other transition metals, confirming uniform Sc doping on the surface of Sc-1. X-ray photoelectron spectroscopy (XPS) was employed to assess the valence states of the elements on the particle surfaces, confirming the presence of Sc in Sc-1, as shown in Fig. S3(a). In addition, using XPS with sputtering depth profiling, we determined that Sc is predominantly distributed within a depth of approximately 10 nm from the surface. High-resolution XPS spectra for Sc-0 (Fig. 1i) and Sc-1 (Fig. 1j) exhibit peaks at 854.26, 855.73, and 862.18 eV, corresponding to Ni^{2+}, Ni^{3+}, and the characteristic satellite peak, respectively, indicating the coexistence of Ni^{2+} and Ni^{3+} in the cathode [31].

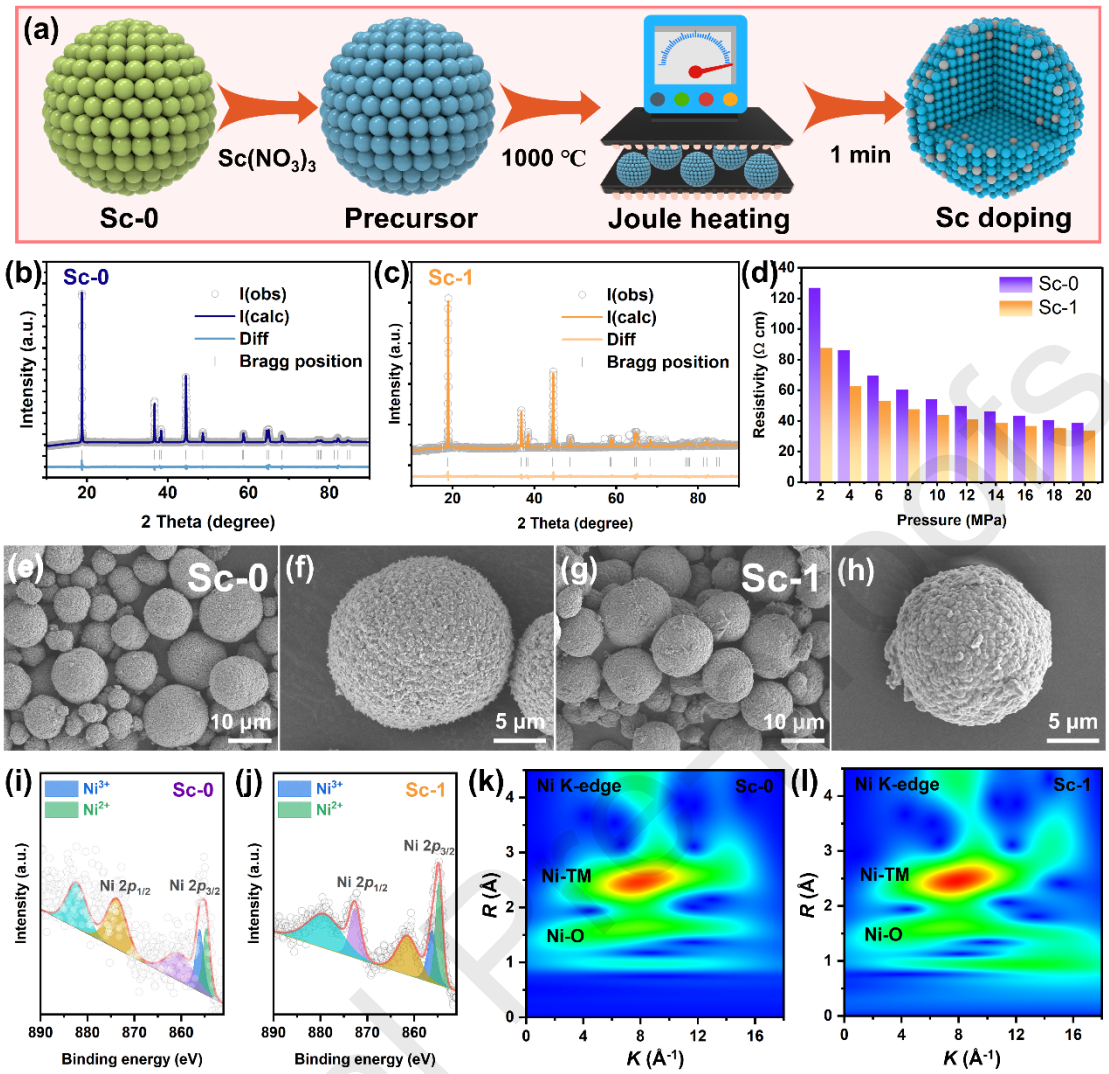

Fig. 1. (a) Schematic illustration of the synthesis of Sc-1. XRD refinement of (b) Sc-0 and (c) Sc-1. (d) Powder resistivity of Sc-0 and Sc-1. SEM images of (e, f) Sc-0 and (g, h) Sc-1. Ni 2*p* XPS spectra of (i) Sc-0 and (j) Sc-1. EXAFS WT images of (k) Sc-0 and (l) Sc-1.

Notably, the electron binding energies of oxygen (Fig. S3b and c) between 528 and 532 eV (Li_2CO_3/LiOH) and between 526 and 528 eV (lattice oxygen) [32] suggest that Sc surface doping enhances the quantity of lattice oxygen while reducing the presence of residual lithium species, indicating that the Sc introduced during the Joule-heating process aids in the consumption of residual lithium [33]. During the Sc surface modification treatment, an extensive washing step effectively removes residual alkaline species such as LiOH and Li_2CO_3 from the cathode surface. These residues are known to react with the electrolyte, leading to oxygen loss and degradation of the surface structure. By removing these impurities, the Sc treatment enhances surface cleanliness and stabilizes the structure, reducing the likelihood of lattice oxygen depletion during cycling. Fig. 1(d) displays consistent signal intensities

for the coordination numbers between the two samples, indicating a shift in the Ni–O bond length toward higher values in Sc-1, which implies a lower Ni oxidation state. This finding, combined with Fourier transform extended X-ray absorption fine structure (FT-EXAFS, Fig. S4) analyses and wavelet transforms (WT) of k^3-weighted EXAFS images (Fig. 1k and l), confirms a longer Ni–O bond in the Sc-1 sample. These results collectively indicate successful Sc doping at the Ni site during the Joule-heating process, leading to a cation mixing layer with a reduced Ni oxidation state and an elongated Ni–O bond.

High-resolution transmission electron microscopy (HRTEM) was utilized to directly examine local structural alterations. Fig. 2(a and b) displays the HRTEM images, fast Fourier transform (FFT) images, and inverse fast Fourier transform (iFFT) images of the pristine Sc-0 and modified Sc-1 samples, respectively. Fig. 2(a) illustrates a purely layered structure extending from the surface to the bulk in the pristine Sc-0 sample. Conversely, Fig. 2(b) indicates that the lattice fringes of Sc-1 are divided into two distinct regions: a thin mixed phase (NiO-like rock salt phase and layered phase) on the surface (designated as region b-1) and a well-defined layered structure in bulk (designated as region b-2). These findings are consistent with the XRD and XPS analyses, suggesting that the reconstruction of the surface mixed phase requires a specific level of Sc doping to achieve an appropriate thickness. The EDS mapping of Sc-1 (Fig. 2c) further substantiates the successful incorporation of Sc into the lattice, demonstrating gradient surface doping. Importantly, the evolution of the lithium-ion concentration gradient is attributed to surface structural disorder. The 8 nm reconstruction layer on the surface, induced by scandium doping, exerts a pinning effect. This effect alleviates the significant *c*-axis contraction resulting from extensive lithium ion removal during deep delithiation and effectively decreases structural degradation from the *R*-3*m* phase to the disordered rock salt phase *Fm*3*m* during cycling. Thus, the cation mixing layer resulting from Sc surface doping functions as a protective barrier for the material throughout cycling, enhancing its durability and performance.

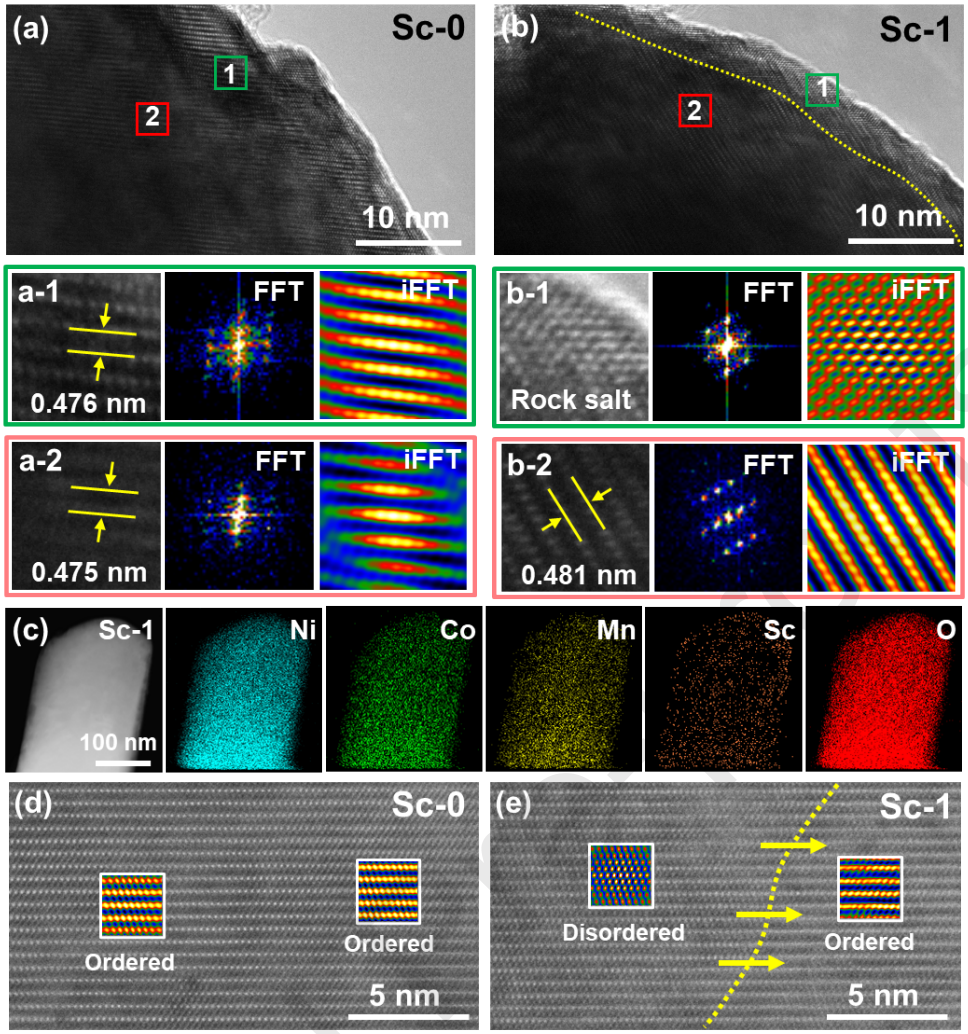

Fig. 2. HRTEM, FFT, and iFFT images of (a) Sc-0 and (b) Sc-1. (c) EDS mapping of Sc-1. HAADF-STEM images of (d) Sc-0 and (e) Sc-1.

To further verify that the disordered cation structure predominates in the surface lattice of the sample, atomic-resolution high-angle annular dark-field (HAADF) scanning transmission electron microscopy (STEM) measurements were conducted. In the HAADF-STEM image, bright spots indicate transition metal (TM) cations with higher atomic numbers, while dark spots represent lithium (Li) with a lower atomic number. This contrast enables HAADF-STEM to differentiate between the cation-ordered layered structure and the cation-disordered structure. Unlike Sc-0 (Fig. 2d and Fig. S5a), the surface region of Sc-1 (Fig. 2e and Fig. S5b) can be broadly divided into two regions delineated by the yellow line. The atomic contrast in the Li layers becomes more pronounced from the surface to the bulk structure along the yellow arrows crossing the yellow line. This transition implies that a disordered layered structure with an increased concentration of Li/Ni antisites near the surface gradually evolves into a well-ordered layered structure with fewer Li/Ni antisites deeper within the bulk [34].

The electrochemical performance was assessed through charge/discharge tests on half-cells at a current density of 1 C (equivalent to 200 mA g^{-1}) within the voltage range of 2.75 to 4.3 V. Fig. 3(a) illustrates the initial charge-discharge curves at 25 °C. Sc-0 exhibits an initial charge capacity of 239.3 mAh g^{-1} and a discharge capacity of 228.8 mAh g^{-1}, resulting in an initial coulombic efficiency (ICE) of 95.61%. In comparison, Sc-1 demonstrates slightly higher charge and discharge capacities of 244.7 and 230.2 mAh g^{-1}, respectively, although the ICE is marginally lower, being 94.07%. The slight reduction in the ICE from 95.61% for the Sc-0 sample to 94.07% for the Sc-1 sample can be attributed to the effects of the Joule-heating process used during the Sc modification. This process involves ultrafast, high-temperature treatment, which, while beneficial for enhancing structural stability, may lead to the volatilization and loss of a small amount of active lithium on the cathode surface. This loss of lithium can reduce the amount of available lithium ions for intercalation during the first charge-discharge cycle, thereby slightly lowering the initial coulombic efficiency. The rate performance of the samples at 25 °C is shown in Fig. 3(b), where both samples generally display a decrease in capacity with increasing current density; however, the capacity of Sc-0 declines more rapidly than that of Sc-1. At a low current density of 0.1 C, Sc-1 achieves an average capacity of 231.7 mAh g^{-1}, which decreases to 196.2 mAh g^{-1} at 3 C, yielding a retention rate of 84.67%. In contrast, Sc-0 records lower average capacities of 226.3 mAh g^{-1} at 0.1 C and 189.7 mAh g^{-1} at 3 C, resulting in a retention rate of 83.82%. Notably, the stable cathodic and anodic peaks in the dQ/dV plots with increasing C rates indicate reduced polarization for Sc-1 (Fig. 3c and Fig. S6a). Fig. 3(d) illustrates the cycling performance of the samples at 25 °C. For Sc-1, the initial discharge capacity at 1 C is 208.1 mAh g^{-1}, and after 100 cycles, the capacity retention is 93.99%, corresponding to a remaining capacity of 195.6 mAh g^{-1}. In comparison, Sc-0 starts with a slightly higher discharge capacity of 209.8 mAh g^{-1}; however, after 100 cycles, it retains only 88.08% of its capacity, equating to 184.8 mAh g^{-1}.

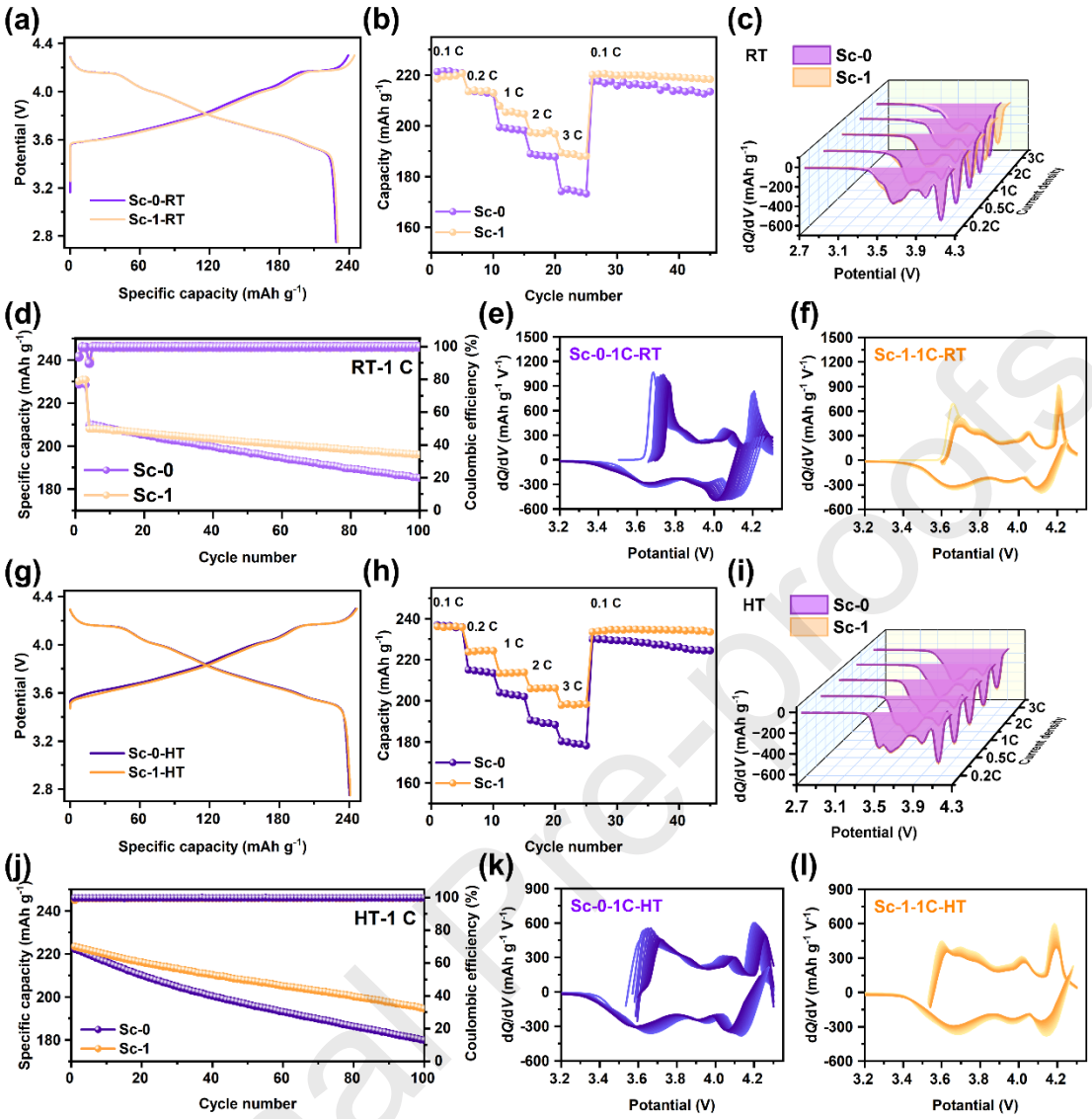

Fig. 3. (a, g) Initial charge-discharge curves, (b, h) rate capabilities, (c, i) differential capacity curves for the discharge processes obtained from rate capability tests under different C rates, and (d, j) cycling performance of different samples at 25 and 50 °C. Long-cycle dQ/dV profiles of (e, k) Sc-0 and (f, l) Sc-1 at 25 and 50 °C.

The dQ/dV profiles (Fig. 3e and f) offer insights into the fading mechanisms. The capacity and voltage degradation observed in the Sc-0 sample are primarily linked to the decreased intensity of the M-H2 and H2-H3 phase transition peaks. Previous studies have indicated that this form of degradation is caused by the interaction of stress fields with chemical reactions, leading to structural instability. Mitigation of this issue can be achieved through cation doping that aids in stabilizing the structure, and by developing a nanoscale cation-mixing layer on the surface to prevent excessive phase transitions [35]. The enhanced cycling stability and lower voltage decay rate of Sc-1 provide additional support for this strategy. The advantages of Sc-1 are

particularly pronounced at elevated temperatures, as demonstrated in Fig. 3(g–l) and Fig. S6(b). At 50 °C, the capacity retention for Sc-1 was 87.06%, while that for Sc-0 was merely 80.96%, indicating the robustness of the electrochemical properties of Sc-1 under thermal stress. This underscores the significance of surface Sc doping and the formation of a nanoscale cation-mixing layer in improving both the rate capability and cycling stability at higher temperatures.

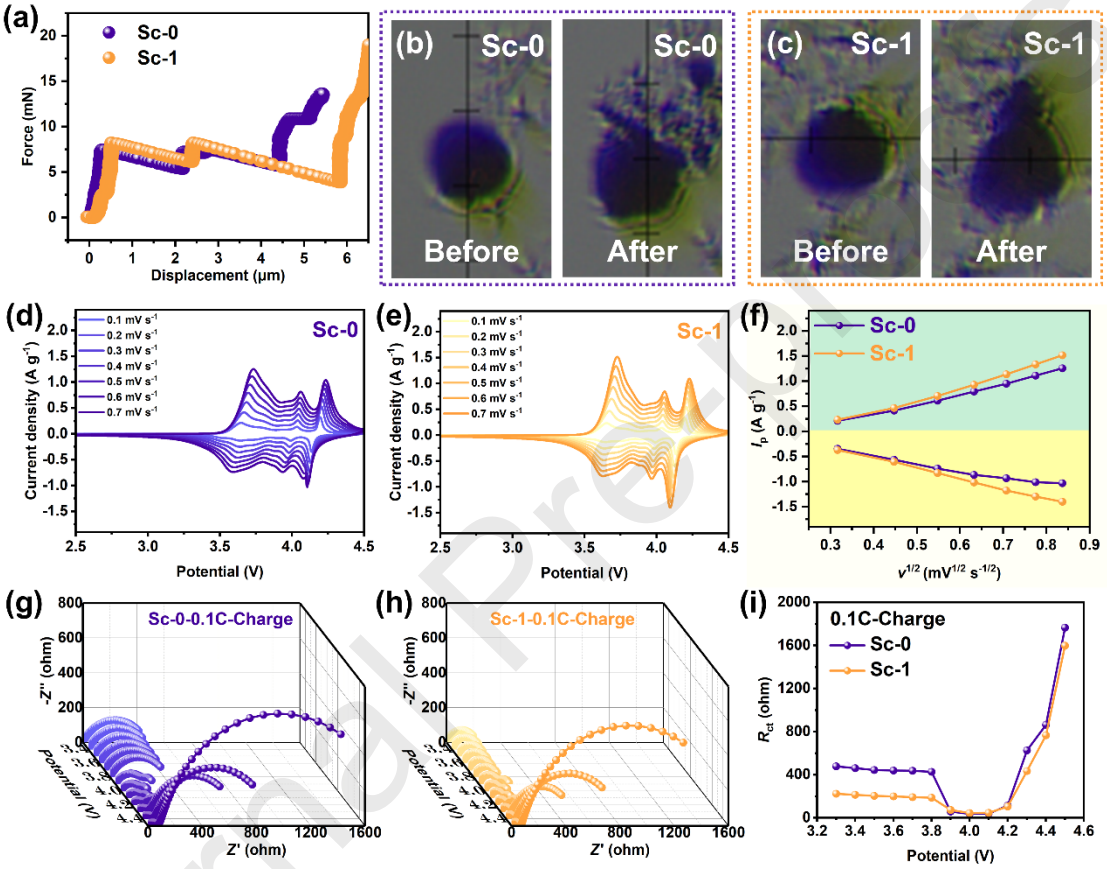

Fig. 4. (a) Single-particle force test. Optical photographs before and after single-particle force testing of the (b) Sc-0 and (c) Sc-1 samples. CV curves of (d) Sc-0 and (e) Sc-1 at 0.1–0.7 mV s^{-1}. (f) The relationship between the scan speed and peak current. In situ EIS results during the initial discharge process for (g) Sc-0 and (h) Sc-1. (i) Corresponding changes in the fitting results of R_{ct}.

Single-particle force tests (IEST, SPFT-2000, Fig. 4a) were performed to assess the mechanical properties and structural stability of the samples. Sc-1 (Fig. 4c) exhibited slightly greater displacement at the crushing point than did Sc-0 (Fig. 4b), indicating that Sc-1 requires deeper compression before fracturing. This enhanced compressive strength of Sc-1 improved the overall electrochemical performance of the battery. Cyclic voltammetry (CV) experiments were conducted at different scan

rates to explore the lithium-ion (Li^+) diffusion capabilities of Sc-0 (Fig. 4d) and Sc-1 (Fig. 4e). By analyzing the peak currents (I_p) from the oxidation and reduction peaks of the CV curves, a linear relationship between the square root of the scan rate ($v^{1/2}$) [36] and the peak current was established, as illustrated in Fig. 4(f). In comparison to the other samples, Sc-1 exhibited a greater Li^+ diffusion coefficient, which correlated with enhanced lithium-ion mobility. This increased diffusion rate significantly contributes to the improved cycling stability observed at elevated current densities, as the improved ion transport minimizes polarization and energy loss during high-rate operation. In situ electrochemical impedance spectroscopy (EIS) measurements further indicated that Sc-1 (Fig. 4g) possesses a lower total resistance than pristine Sc-0 (Fig. 4 h), with reduced fluctuations in charge transfer impedance (R_{ct}, Fig. 4i), suggesting superior interfacial stability and enhanced charge transfer dynamics.

To quantify the impact of Sc incorporation on the anisotropic lattice structure distortion, the structural evolution of the Sc-0 and Sc-1 electrodes was examined through in situ XRD during the initial charging process at a current of 0.2 C. Fig. 5(a and b) presents contour plots of selected regions of the in situ XRD patterns for both samples during charging, emphasizing the evolution of key diffraction peaks. The movement of the (003) peak indicates variations in the *c*-axis lattice parameter, while the shift of the (110) peak reflects changes in the *a*-axis lattice parameter. In the Sc-1 sample (Fig. 5b), the (003) peak shifts consistently by a maximum of 0.82° during charging, accompanied by a gradual phase transition through the H1, H2, and H3 phases. This smooth transition contrasts sharply with the abrupt shift of the (003) peak seen in Sc-0 (Fig. 5a), which achieves a maximum shift of 1.02°, indicating more significant lattice distortion in the absence of scandium incorporation. The reduced peak shift in Sc-1 suggests that the surface Sc doping effectively moderates the phase transitions, thereby enhancing structural stability.

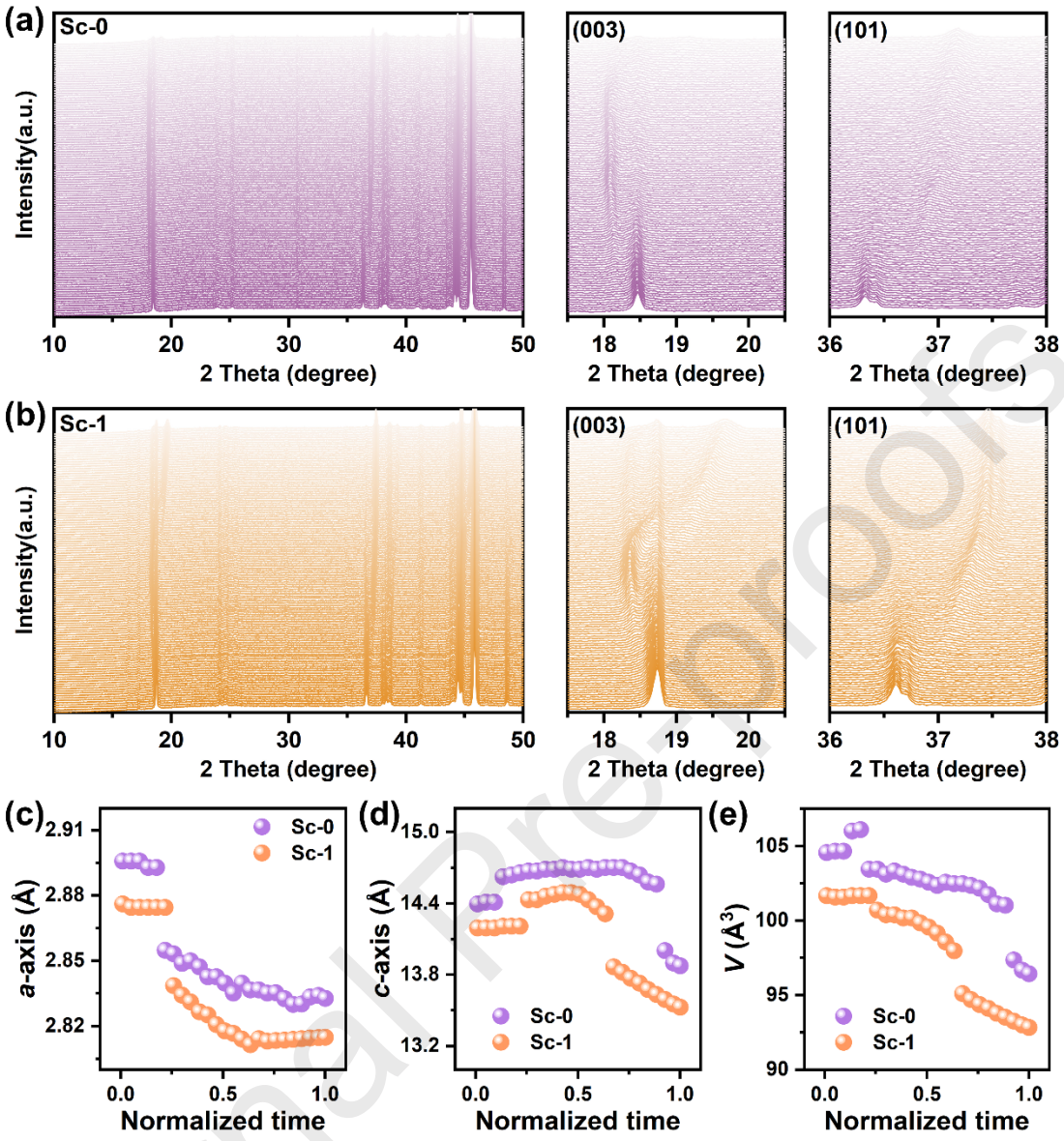

Fig. 5. Stacked profiles of the in situ XRD patterns and corresponding (003) peak and (101) profiles for (a) Sc-0 and (b) Sc-1. The corresponding (c) *a*-axis lattice parameters, (d) *c*-axis lattice parameters, and (e) unit cell volume variations.

Further analysis of the lattice parameters (*a* and *c*) for both Sc-0 and Sc-1 is depicted in Fig. 5(c and d). Both samples display a similar trend in lattice parameter variation. The *a*-lattice parameter decreases progressively throughout charging, attributed to the oxidation of nickel ions. Additionally, the *c*-lattice parameter expands during the initial stages of charging but sharply decreases at about 70% state of charge (SOC), coinciding with the removal of a significant quantity of lithium ions from the crystal structure. However, the changes in the lattice parameters of Sc-1 were more controlled. Specifically, Sc-1 exhibited Δa and Δc values of 1.94% and 1.40%, respectively, resulting in a total volume change (ΔV) of 5.2% (Fig. 5e). In contrast,

the lattice parameter changes in Sc-0 were more pronounced, with Δ*a* of 1.96%, Δ*c* of 3.59%, and Δ*V* of 5.57%. The smaller lattice distortions in Sc-1 indicate that Sc incorporation plays a vital role in facilitating a more controlled phase transition, enhancing the reversibility of these transitions and reducing anisotropic lattice distortion. This behavior can be attributed to the improved structural stability during lithium insertion and removal, preventing excessive lattice deformation. Overall, the findings underscore the effectiveness of surface Sc doping in enhancing the mechanical and electrochemical performance of the electrode by preserving structural integrity during cycling.

The enhanced chemomechanical stability of the Sc-1 cathode was confirmed following extended cycling. SEM images and EDS maps (Fig. S7) indicate that after prolonged cycling, Sc-0 fragments into smaller particles and accumulates byproduct deposits from side reactions. In contrast, Sc-1 preserves its structural integrity and experiences fewer side reactions. Fig. S8 further supports the improved structural and thermal stability of Sc-1 after high-temperature cycling. As illustrated in Fig. 6(a), the cross-sectional view of the Sc-0 cathode after 100 charge/discharge cycles reveals significant microcrack formation and propagation. These microcracks suggest mechanical degradation during repeated lithiation and delithiation processes, ultimately resulting in reduced structural integrity. Fig. 6(b) demonstrates extensive growth of the rock-salt phase in the Sc-0 cathode, which arises from continuous reactions with the electrolyte during cycling. This phase formation results from the destabilized surface structure, which becomes more reactive and develops undesirable phases as cycling continues. In contrast, the Sc-1 cathode displayed markedly enhanced structural integrity. Fig. 6(c and d) indicates that microcrack propagation and rock-salt phase expansion are effectively inhibited in Sc-1. This enhancement is primarily attributed to the surface restructuring induced by Sc doping, which accommodates the lattice contraction and expansion occurring during cycling.

Particle pulverization and surface degradation contribute to the acceleration of cathode impedance growth [37,38]. As depicted in Fig. S9, EIS testing demonstrates that Sc-1 particles exhibit significantly lower charge transfer resistance (R_{ct}) growth compared to bare Sc-0 cathodes at both 25 and 50 °C, highlighting the effectiveness of the dual strategy in enhancing interfacial charge transfer and improving electrochemical performance. The surface chemical composition was further analyzed using time-of-flight secondary ion mass spectrometry (TOF-SIMS). Examination of both samples revealed that their CEI consists of an outer layer of organic species and an inner layer of inorganic species. TOF-SIMS results indicated that the intersection between the curves for organic species (CH_2O^-) and inorganic species (NiF_3^-) occurred significantly earlier in Sc-1 (Fig. 6f and Fig. S10b) than that in Sc-0 (Fig. 6e and Fig. S10a), suggesting a thinner CEI layer in Sc-1. This reduced thickness indicates fewer side reactions between the Sc-1 cathode and the electrolyte. Conversely, the CEI of Sc-0 was notably thicker, containing greater quantities of both CH_2O^- and NiF_3^-. This increased thickness results from intensified side reactions between Sc-0 and the electrolyte, leading to continuous nickel dissolution and

excessive electrolyte consumption. In Sc-1, the CH_2O^- and NiF_3^- layers were thinner and less pronounced, indicating that the surface restructuring induced by Sc doping effectively mitigated nickel dissolution and electrolyte decomposition. This restructuring facilitates the formation of a more compact, thin, and stable CEI film, thereby enhancing the long-term stability and performance of the Sc-1 cathode [39].

The surface electronic structure of nickel in the cathodes after 100 cycles was investigated using Ni *L*-edge soft XAS in surface-sensitive total electron yield (TEY) mode. As illustrated in Fig. 6(g), the ratio of L_3(high) to L_3(low) offers insights into the oxidation state of nickel, with higher L_3(high)/L_3(low) ratios indicative of an elevated oxidation state. Following 100 cycles, the L_3(high)/L_3(low) ratio of the Sc-0 cathode decreased to 0.304. This reduction indicates a significant accumulation of Ni^{2+} on the surface, alongside a notable transition from the desired layered structure to the undesirable rock-salt phase. This phase transition adversely affects electrochemical performance and underscores the structural instability of the Sc-0 sample after extended cycling. In contrast, the elevated L_3(high)/L_3(low) ratios observed in the cycled Sc-1 sample suggest enhanced stability of the nickel oxidation state, indicating that Sc-1 more effectively maintains the layered structure compared to Sc-0 after cycling. This finding aligns with the improved structural integrity noted in Sc-1, where surface restructuring induced by Sc doping mitigates phase transitions and enhances overall electrochemical stability.

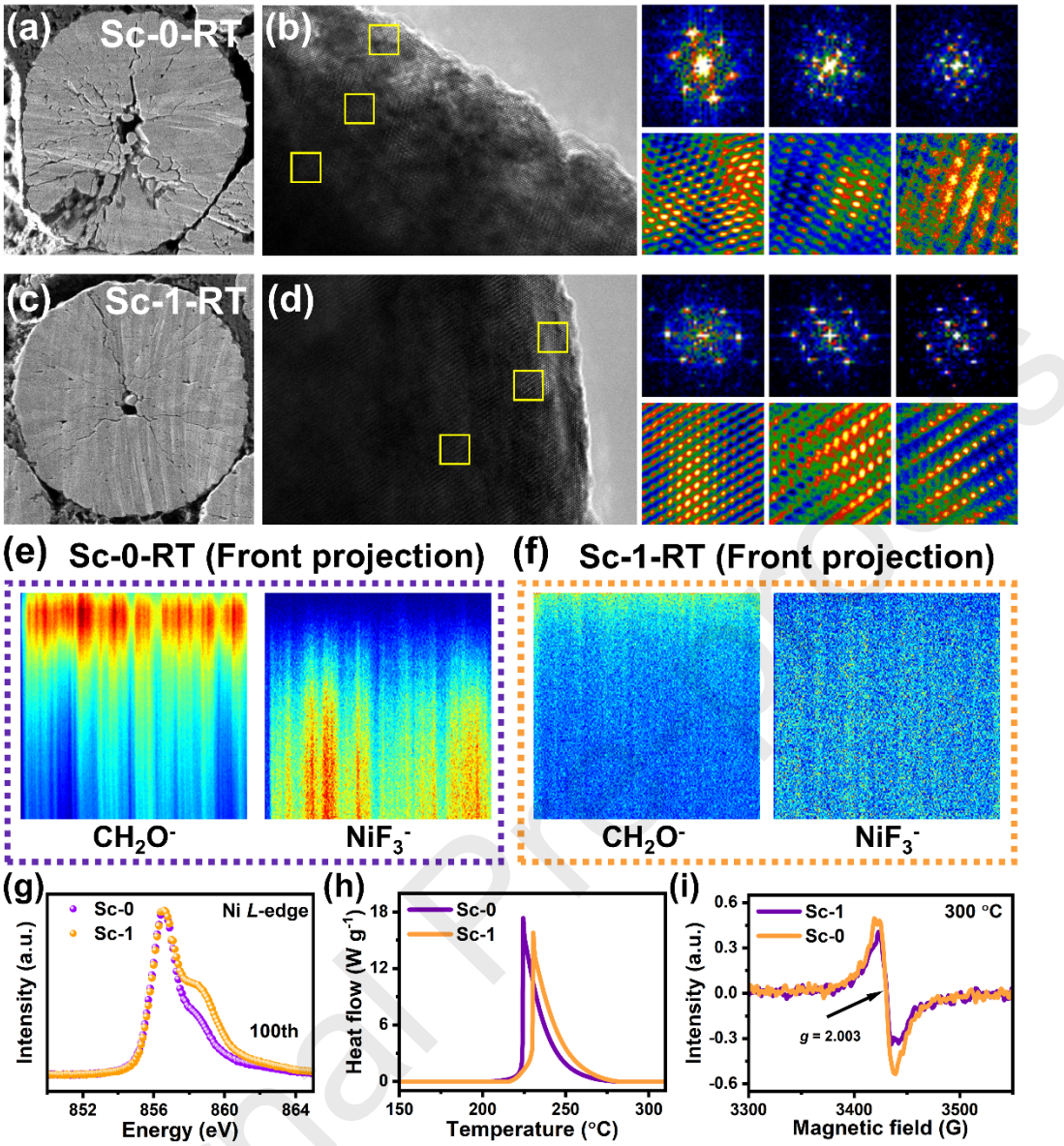

Fig. 6. Post-cycle characterization after 100 cycles at 1 C. (a) Cross-sectional SEM image of Sc-0. (b) HRTEM and FFT/iFFT images of Sc-0. (c) Cross-sectional SEM image of Sc-1. (d) HRTEM and FFT/iFFT images of Sc-1. TOF-SIMS plots of (e) Sc-0 and (f) Sc-1. (g) Soft XAS spectra of the Ni *L*-edge in TEY mode. (h) DSC profiles after charging to 4.3 V. (i) EPR spectra after heating at 200 °C for 10 min.

Thermal stability was assessed using differential scanning calorimetry (DSC). DSC profiles were recorded after the electrodes were charged to 4.3 V in the presence of electrolytes. As illustrated in Fig. 6(h), the onset temperature for oxygen evolution in the Sc-1 sample was found to be higher (195.0 °C) compared to that of the Sc-0 sample (184.4 °C), and the total heat release was markedly lower (114.36 versus 216.01 J g^{-1}). These findings indicate that the Sc-1 sample exhibits greater thermal stability than the Sc-0 sample, with decreased heat generation and a delayed onset of

oxygen release, which is essential for improving the safety of the cathode during operation at elevated temperatures [40]. Alongside the DSC analysis, electron paramagnetic resonance (EPR) spectroscopy offered additional confirmation of the enhanced structural and thermal stability of Sc-1. Following heating to 200 °C for 10 min, the EPR spectra (Fig. 6i) displayed a decreased signal intensity at g = 2.003 for Sc-1, suggesting a reduced concentration of oxygen vacancies relative to the Sc-0 sample. Oxygen vacancies in cathode materials are frequently linked to structural degradation and heightened reactivity, especially at elevated temperatures. The lower occurrence of oxygen vacancies in Sc-1 indicates that its lattice oxygen remains more stable under thermal stress, thereby further affirming the superior thermal resilience of Sc-1 when compared to Sc-0. Collectively, the enhanced surface stability, reduced phase transitions, and improved thermal properties in the Sc-1 sample underscore the advantageous effects of surface doping and structural modifications on both electrochemical performance and safety.

DFT calculations were performed to assess the formation energies of potential Sc dopant configurations. Based on the Sc-0 structure (Fig. 7a), Sc substitution for Li sites (Fig. 7b) and Ni sites (Fig. 7c) was evaluated. The results presented in Fig. 7(e) demonstrate that Sc substitution at Ni sites (−11.972 eV) yields significantly lower formation energies compared to those at Li sites (−10.577 eV), indicating that doping Sc into the TM layer represents the most energy-efficient configuration. Furthermore, based on the XRD refinement and HAADF-STEM analysis previously described, a Li/Ni antisite defect was incorporated into the Sc-Ni model to form the Sc-Ni/Li structure. The calculated formation energy for this configuration was −13.324 eV, confirming the structural stability of the Sc-Ni/Li model in the presence of Li/Ni antisite defects. Additionally, formation energies of the oxygen vacancies were calculated for various configurations to evaluate the impact of Sc doping on the stability of the lattice oxygen environment. The atomic configurations of the oxygen vacancies are illustrated in Fig. 7(f). The formation energy of the oxygen vacancies in the Sc-Ni/Li structure is significantly higher than that in the Sc-0 and Sc-Ni structures, indicating that Sc doping greatly enhances the stability of lattice oxygen in the Sc-Ni/Li configuration, thereby decreasing the probability of oxygen vacancy formation.

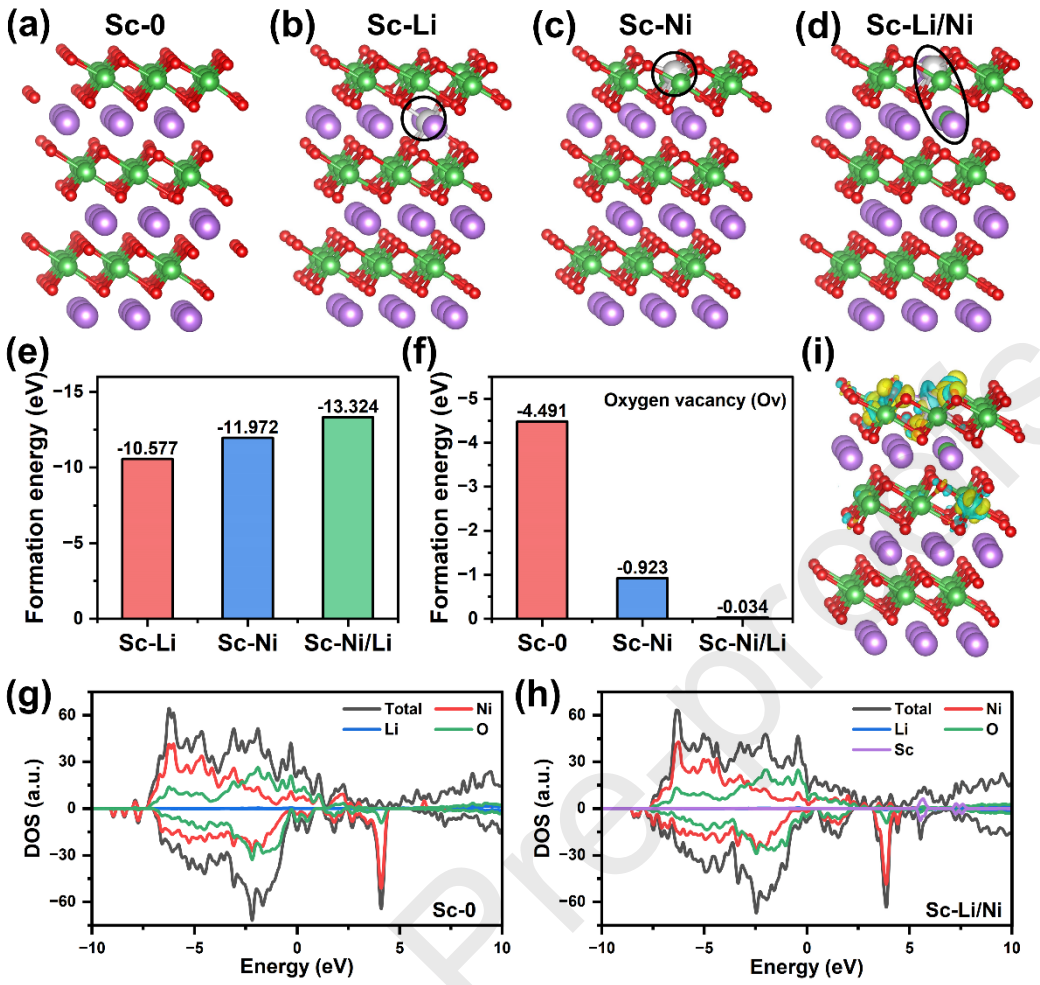

Fig. 7. Schematic diagram of (a) Sc-0, (b) Sc-Li, (c) Sc-Ni, and (d) Sc-Ni/Li. (e) Formation energies of different structures and (f) Comparison of the formation energies of oxygen vacancies. Density of states for (g) Sc-0 and (h) Sc-Ni/Li. (i) Differential charge density analysis for Sc-Ni/Li.

The impact of Sc incorporation on the electronic structure was further investigated through density of states (DOS) analysis. The DOS diagrams reveal that the electronic states in Sc-0 (Fig. 7g) primarily originate from the hybridization of Ni 3*d* and O 2*p* orbitals. The contribution of Sc doping to the overall DOS is minimal; however, new peaks appear in the energy ranges of 0.6–2.6 eV and 4.9–7.2 eV in the Sc-Ni/Li structure (Fig. 7h), which are not present in the pristine Sc-0 configuration. These additional peaks suggest that the incorporation of Sc induces slight lattice distortions. Notably, the DOS near the Fermi level (EF) is primarily contributed by Ni and O due to strong TM-oxygen interactions. The incorporation of Sc^{3+} and Li/Ni antisite defects in the Sc-Ni/Li structure increases the DOS near the EF, increasing the number of electrons in this region. Increased electron density near the EF contributes to a reduction in the band gap and an enhancement of electronic conductivity, which are crucial for improving the electrochemical performance of the cathode material.

This modification is supported by the differential charge density analysis presented in Fig. 7(i). The analysis demonstrated a greater electronic polarization between Sc and O compared to that between Ni and O in the Sc-Ni/Li structure, indicating that the Sc–O bond exhibits more stability than the Ni–O bond. The formation of these more robust Sc–O bonds is significant for improving the structural stability of the cathode. In conclusion, the introduction of Sc into the TM layer of the ultrahigh-Ni cathode promotes the formation of more stable Sc–O bonds, decreases the creation of oxygen vacancies, and enhances the overall structural integrity and electronic conductivity, as confirmed by DFT calculations, DOS analysis, and differential charge density results.

Simulation results reveal the impact of Li-ion concentration distribution and surface stress (Fig. 8). In the initial charge-discharge cycle of the unmodified Sc-0 sample, a reduced Li-ion diffusion coefficient causes significant concentration disparities, with higher ion concentration in the bulk than on the surface. This difference leads to severe stress gradients, especially under high cut-off voltages during prolonged cycling [41,42]. Conversely, the Sc-modified sample exhibits improved diffusion capabilities, resulting in a more uniform concentration distribution with reduced stress gradients. Even after extended cycling, the Sc-modified sample maintains a stable concentration profile. This enhanced performance is attributed to synergistic effects of surface restructuring and cation mixing, which increase the diffusion coefficient, thereby supporting efficient ion transport and prolonged material stability.

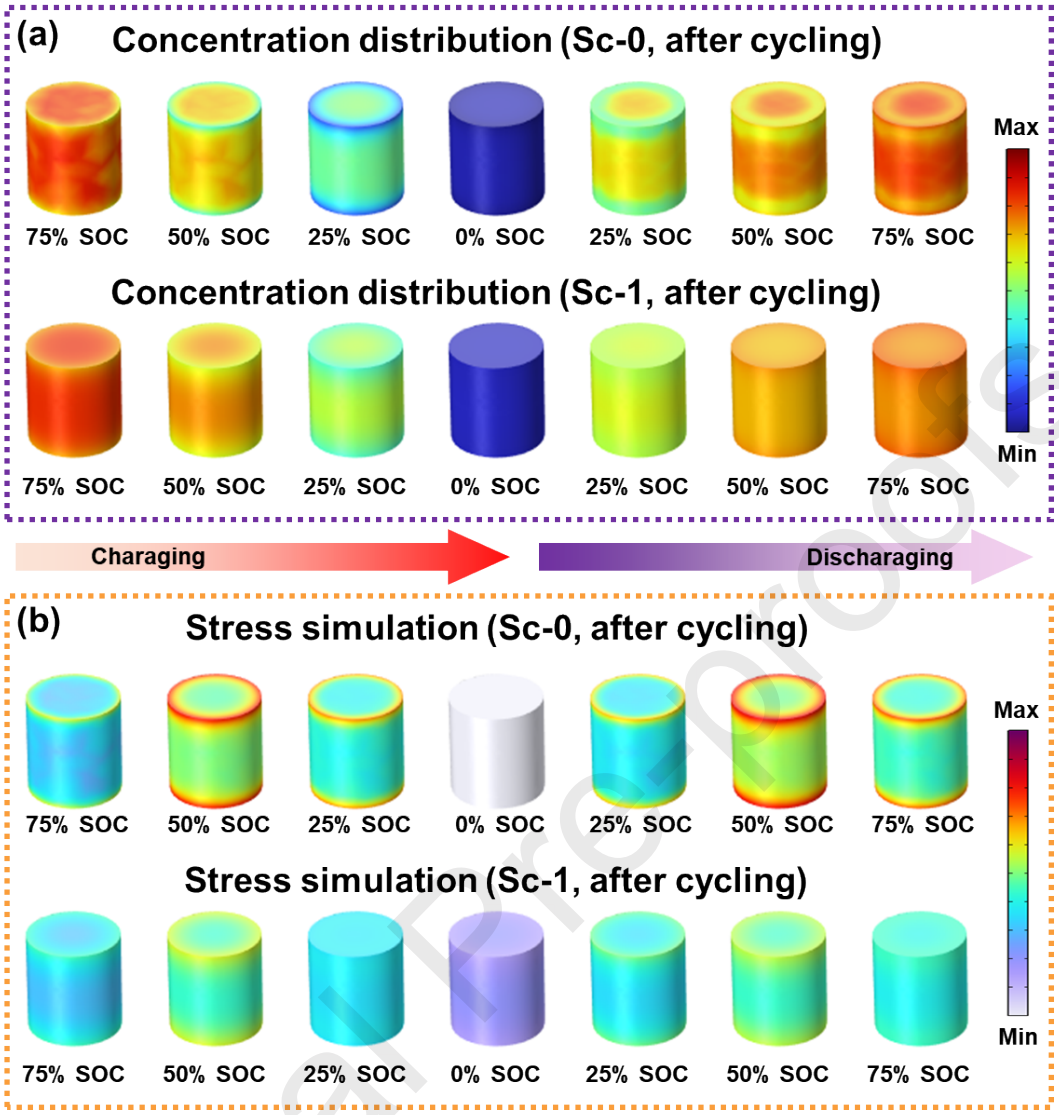

Fig. 8. The simulation diagram of (a) lithium ion concentration distribution and (b) stress.

A comprehensive analysis of ultrahigh-Ni cathode materials indicated that the Sc-0 cathode experiences notable electrochemical and mechanical instability, especially during deep charging cycles. The H2-H3 phase transition represents one of the main challenges, as it instigates lattice oxygen instability, which induces heterogeneous mechanical strain throughout the cathode particles. This strain, along with irreversible structural alterations, accelerates particle cracking and results in surface phase transformations detrimental to the long-term performance of the cathode. These structural and phase instabilities significantly hinder the kinetics of lithium-ion transport, leading to considerable capacity fading during extended cycling. Furthermore, the instability of lattice oxygen contributes to side reactions at the cathode-electrolyte interface, particularly under elevated temperature conditions, worsening capacity decay and further compromising electrochemical performance.

These issues can be alleviated through the strategic combination of Sc surface doping and the incorporation of a cation-mixing layer. This approach facilitates several advantageous processes: atomic reconstruction, grain rearrangement, and interface shielding. Collectively, these processes mitigate the undesirable H2-H3 phase transition and lessen interfacial side reactions by stabilizing the cathode surface. Additionally, the cation-mixing layer enhances uniform strain distribution across the particles and promotes Li^+ migration, ensuring more effective ion transport during cycling. Consequently, the cycling durability and Li^+ diffusion kinetics of the cathode are significantly enhanced. The improved mechanical integrity, resulting from the prevention of particle cracking, along with the chemical stability of the cathode material, contributes to its long-term performance, rendering this strategy highly effective for stabilizing ultrahigh-Ni cathodes during prolonged cycling and under demanding conditions such as elevated temperatures.

3. Conclusions

In this study, it is shown that doping-induced surface restructuring in ultrahigh-nickel cathode materials can be achieved within seconds through an ultrafast Joule heating method. This approach facilitates the rapid synthesis of cathode materials while allowing for control over critical structural features that enhance their electrochemical performance. During the Sc surface doping process, a strategically introduced electrochemically inert cation-mixing layer is incorporated into the layered structure. The nonequilibrium environment created by the ultrafast Joule heating process is pivotal in promoting this restructuring, which notably improves the stability of the structure/interface and the mechanical integrity of the ultrahigh-Ni layered cathode. Sc doping exhibits a "pinning effect" on the grain boundaries of the cathode particles, which is essential for improving Li^+ diffusion kinetics by reducing mechanical strain experienced by the cathode during cycling. By facilitating quicker Li^+ migration, the material can sustain higher charge and discharge rates, enhancing overall performance. Furthermore, the in situ formation of a cation-mixing layer at grain boundaries establishes a robust cathode/electrolyte interphase, which is crucial for minimizing unwanted interfacial reactions. Specifically, this protective layer suppresses parasitic reactions between the cathode and electrolyte and prevents the dissolution of transition metals (TMs) during operation. Advanced characterization techniques, including STEM and TOF-SIMS, confirm reduced TM dissolution in the modified cathode. Consequently, these synergistic modifications result in Sc doping alleviating particle cracking and minimizing surface and interface degradation, thereby enhancing rate capability, structural robustness, and thermal stability. In conclusion, this work introduces an innovative and efficient design and synthesis strategy for creating low-cost, high-performance cathode materials. This combination of benefits is particularly significant for applications demanding high energy density and operational stability, such as electric vehicle batteries.

Experimental section

Experimental details can be found in the Supporting Information.

Acknowledgments

This research was supported by the National Key R&D Program of China (2022YFB3803501), the National Natural Science Foundation of China (22179008, 22209156). L. Chen acknowledges the support from the Beijing Nova Program (20230484241). J.Y. Dong acknowledges the support from the China Postdoctoral Science Foundation (2024M754084) and the Postdoctoral Fellowship Program of CPSF (GZB20230931). The authors thank the support from beamline BL08U1A of Shanghai Synchrotron Radiation Facility (2024-SSRF-PT-506950), beamline 1W1B of the Beijing Synchrotron Radiation Facility (2021-BEPC-PT-006276). The authors also thank for the support from Initial Energy Science & Technology Co., Ltd (IEST).

References

[1] J. Xiao, F. Shi, T. Glossmann, C. Burnett, Z. Liu, Nat. Energy 8 (2023) 329-339.

[2] J. Lin, X. Zhang, E. Fan, R. Chen, F. Wu, L. Li, Energy Environment. Sci. 16 (2023) 745-791.

[3] Y. Chen, Y. Kang, Y. Zhao, L. Wang, J. Liu, Y. Li, Z. Liang, X. He, X. Li, N. Tavajohi, B. Li, J. Energy Chem. 59 (2021) 83-99.

[4] A. Manthiram, Nat. Commun. 11 (2020) 1550.

[5] M. Li, J. Lu, Z. Chen, K. Amine, Adv. Mater. 30 (2018) 1800561.

[6] B. E. Murdock, K. E. Toghill, N. Tapia-Ruiz, Adv. Energy Mater. 11 (2021) 2102028.

[7] J. Wang, X. Lu, Y. Zhang, J. Zhou, J. Wang, S. Xu, J. Energy Chem. 65 (2022) 681-687.

[8] L. Shen, J.-L. Li, W.-J. Kong, C.-X. Bi, P. Xu, X.-Y. Huang, W.-Z. Huang, F. Fu, Y.-C. Le, C.-Z. Zhao, H. Yuan, J.-Q. Huang, Q. Zhang, Adv. Funct. Mater. (2024) 2408571.

[9] Y. Zou, Y.L. Tang, S.Y. Zhou, H.T. Zhang, J.K. Chen, Y.W. Yan, H. Cao, J.P. Xu, W. Yin, H-G Liao, Y. Qiao, J. Bao, S-G. Sun, Energy Storage Mater. 69 (2024)

103400.

[10] Y. Su, Q. Zhang, L. Chen, L. Bao, Y. Lu, S. Chen, F. Wu, J. Energy Chem. 65 (2022) 236-253.

[11] F. Wu, N. Liu, L. Chen, Y. Su, G. Tan, L. Bao, Q. Zhang, Y. Lu, J. Wang, S. Chen, J. Tan, Nano Energy 59 (2019) 50-57.

[12] F. Wu, J. Dong, L. Chen, L. Bao, N. Li, D. Cao, Y. Lu, R. Xue, N. Liu, L. Wei, Z. Wang, S. Chen, Y. Su, Energy Storage Mater. 41 (2021) 495-504.

[13] S. Yin, W. Deng, J. Chen, X. Gao, G. Zou, H. Hou, X. Ji, Nano Energy 83 (2021) 105854.

[14] Q. Huang, X. Zhang, F. Wu, R. Chen, L. Li, Energy Storage Mater. 63 (2023) 103050.

[15] Y. Song, Y. Cui, L. Geng, B. Li, L. Ge, L. Zhou, Z. Qiu, J. Nan, W. Wu, H. Xu, X. Li, Z. Yan, Q. Xue, Y. Tang, W. Xing, Adv. Energy Mater. 14 (2024) 2303207.

[16] S. Zhang, J. Wu, N. Jiang, H. Sun, H. Yang, L. Shen, M. Zhou, W. Liu, H. Zhou, H. Zhao, Adv. Energy Mater. 14 (2024) 2401123.

[17] Z. Dai, Y. Liu, X. Lu, H. Zhao, Y. Bai, Adv. Mater. 36 (2024) 2313500.

[18] Y. Chu, Y. Mu, L. Zou, Y. Hu, J. Cheng, B. Wu, M. Han, S. Xi, Q. Zhang, L. Zeng, Adv. Mater. 35 (2023) 2212308.

[19] N.-Y. Park, S.-B. Kim, M.-C. Kim, S.-M. Han, D.-H. Kim, M.-S. Kim, Y.-K. Sun, Adv. Energy Mater. 13 (2023) 2301530.

[20] X. Ou, T. Liu, W. Zhong, X. Fan, X. Guo, X. Huang, L. Cao, J. Hu, B. Zhang, Y. S. Chu, G. Hu, Z. Lin, M. Dahbi, J. Alami, K. Amine, C. Yang, J. Lu, Nat. Commun. 13 (2022) 2319.

[21] S.-B. Lee, N.-Y. Park, G.-T. Park, U.-H. Kim, S.-J. Sohn, M.-S. Kang, R. M. Ribas, R. S. Monteiro, Y.-K. Sun, ACS Energy Lett. 9 (2024) 740-747.

[22] A. Saleem, L. L. Shaw, R. Iqbal, A. Hussain, A. R. Akbar, B. Jabar, S. Rauf, M. K. Majeed, Energy Storage Mater. 69 (2024) 103440.

[23] M.-Y. Qi, S.-D. Zhang, S. Guo, P.-X. Ji, J.-J. Mao, T.-T. Wu, S.-Q. Lu, X. Zhang, S.-G. Chen, D. Su, G.-H. Chen, A.-M. Cao, Small Methods 7 (2023) 2300280.

[24] Y. Zou, Y. Tang, Q. Zheng, H. Zhang, Y. Yan, J. Xue, S. Zhou, J. Xu, W. Yin, H.-G. Liao, Y. Qiao, J. Bao, S.-G. Sun, Adv. Funct. Mater. (2024) 2406068.

[25] F. Wu, N. Liu, L. Chen, N. Li, J. Dong, Y. Lu, G. Tan, M. Xu, D. Cao, Y. Liu, Y.

Chen, Y. Su, J. Energy Chem. 62 (2021) 351-358.

[26] W. Zhu, J. Zhang, J. Luo, C. Zeng, H. Su, J. Zhang, R. Liu, E. Hu, Y. Liu, W.-D. Liu, Y. Chen, W. Hu, Y. Xu, Adv. Mater. 35 (2023) 2208974.

[27] J. Luo, J. Zhang, Z. Guo, Z. Liu, C. Wang, H. Jiang, J. Zhang, L. Fan, H. Zhu, Y. Xu, R. Liu, J. Ding, Y. Chen, W. Hu, Adv. Mater. 36 (2024) 2405956.

[28] W. Chen, Y. Cheng, J. Chen, K. V. Bets, R. V. Salvatierra, C. Ge, J. T. Li, D. X. Luong, C. Kittrell, Z. Wang, E. A. McHugh, G. Gao, B. Deng, Y. Han, B. I. Yakobson, J. M. Tour, Nat. Commun. 15 (2024) 6250.

[29] W. Zhu, H. Su, P. Bai, Z. Li, J. Zhang, J. Zhang, M. Li, Y. Chen, Y. Xu, Chem. Eng. J. 480 (2024) 148045.

[30] Y. Liu, Q. Wang, L. Chen, Z. Xiao, X. Fan, S. Ma, L. Ming, A. Tayal, B. Zhang, F. Wu, X. Ou, Mater. Today 61 (2022) 40-53.

[31] L. Qiu, W. Xiang, W. Tian, C.-L. Xu, Y.-C. Li, Z.-G. Wu, T.-R. Chen, K. Jia, D. Wang, F.-R. He, X.-D. Guo, Nano Energy 63 (2019) 103818.

[32] H.-H. Ryu, H.-W. Lim, S. G. Lee, Y.-K. Sun, Nat. Energy 9 (2023) 47-56.

[33] J. Li, W. Zhong, Q. Deng, Q. Zhang, Z. Lin, C. Yang, Adv. Funct. Mater. 33 (2023) 2300127.

[34] S. Jamil, C. Li, M. Fasehullah, P. Liu, F. Xiao, H. Wang, S. Bao, M. Xu, Energy Storage Mater. 45 (2022) 720-729.

[35] X. Ou, T. Liu, W. Zhong, X. Fan, X. Guo, X. Huang, L. Cao, J. Hu, B. Zhang, Y. S. Chu, G. Hu, Z. Lin, M. Dahbi, J. Alami, K. Amine, C. Yang, J. Lu, Nat. Commun. 13 (2022) 2319.

[36] X. Zhang, T. Wu, J. Jian, S. Lin, D. Sun, G. Fu, Y. Xu, Z. Liu, S. Li, H. Huo, Y. Ma, G. Yin, P. Zuo, X. Cheng, C. Du, Small 20 (2024) 2404488.

[37] N.-Y. Park, G.-T. Park, S.-B. Kim, W. Jung, B.-C. Park, Y.-K. Sun, ACS Energy Lett. 7 (2022) 2362-2369.

[38] N. S. Luu, K.-Y. Park, M. C. Hersam, Acc. Mater. Res. 3 (2022) 511-524.

[39] J. Dong, F. Wu, J. Zhao, Q. Shi, Y. Lu, N. Li, D. Cao, W. Li, J. Hao, X. Yang, L. Chen, Y. Su, Energy Storage Mater. 60 (2023) 102798.

[40] J. Shen, B. Zhang, W. Huang, X. Li, Z. Xiao, J. Wang, T. Zhou, J. Wen, T. Liu, K. Amine, X. Ou, Adv. Funct. Mater. 33 (2023) 2300081.

[41] W. Wang, Z. Xiao, J. Liu, X. He, J. Wen, Y. Zhou, L. Cheng, B. Zhang, T. Liu,

K. Amine, X. Ou, Adv. Funct. Mater. (2024). Doi: 10.1002/adfm.202409956.

[42] W. Wang, Y. Zhou, B. Zhang, W. Huang, L. Cheng, J. Wang, X. He, L. Yu, Z. Xiao, J. Wen, T. Liu, K. Amine, X. Ou, ACS Nano 18 (2024) 8002-8016.

Graphical Abstract

Ultrafast Joule heating enables Sc doping-induced surface restructuring in ultrahigh-nickel cathodes, forming a cation-mixing layer that enhances structural stability, Li^+ diffusion, and electrochemical performance, addressing challenges in high-energy-density battery applications.

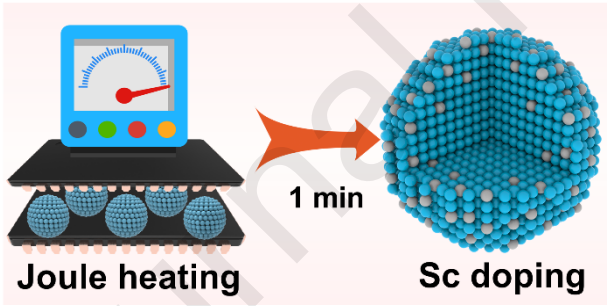

Declaration of interests

☒ The authors declare that they have no known competing financial interests or personal relationships that could have appeared to influence the work reported in this paper.

☐The authors declare the following financial interests/personal relationships which may be considered as potential competing interests: